

This is an Open Access document downloaded from ORCA, Cardiff University's institutional repository: <https://orca.cardiff.ac.uk/id/eprint/123148/>

This is the author's version of a work that was submitted to / accepted for publication.

Citation for final published version:

Zunic, Jovisa and Rosin, Paul L. 2020. Measuring shapes with desired convex polygons. IEEE Transactions on Pattern Analysis and Machine Intelligence 42 (6) 10.1109/TPAMI.2019.2898830

Publishers page: <http://dx.doi.org/10.1109/TPAMI.2019.2898830>

Please note:

Changes made as a result of publishing processes such as copy-editing, formatting and page numbers may not be reflected in this version. For the definitive version of this publication, please refer to the published source. You are advised to consult the publisher's version if you wish to cite this paper.

This version is being made available in accordance with publisher policies. See <http://orca.cf.ac.uk/policies.html> for usage policies. Copyright and moral rights for publications made available in ORCA are retained by the copyright holders.



Measuring Shapes with Desired Convex Polygons

Joviša Žunić, Paul L. Rosin

Abstract—In this paper we have developed a family of shape measures. All the measures from the family evaluate the degree to which a shape looks like a predefined convex polygon. A quite new approach in designing object shape based measures has been applied. In most cases such measures were defined by exploiting some shape properties. Such properties are optimized (e.g. maximized or minimized) by certain shapes and based on this, the new shape measures were defined. An illustrative example might be the shape circularity measure derived by exploiting the well-known result that the circle has the largest area among all the shapes with the same perimeter. Of course, there are many more such examples (e.g. ellipticity, linearity, elongation, and squareness measures are some of them). There are different approaches as well. In the approach applied here, no desired property is needed and no optimizing shape has to be found. We start from a desired convex polygon, and develop the related shape measure. The method also allows a tuning parameter. Thus, there is a new 2-fold family of shape measures, dependent on a predefined convex polygon, and a tuning parameter, that controls the measure's behavior. The measures obtained range over the interval $(0, 1]$ and pick the maximal possible value, equal to 1, if and only if the measured shape coincides with the selected convex polygon that was used to develop the particular measure. All the measures are invariant with respect to translations, rotations, and scaling transformations. An extension of the method leads to a family of new shape convexity measures.

Index Terms—Shape, shape descriptors, shape measure, shape convexity, image processing, pattern recognition.



1 INTRODUCTION

Shape is an object property with a powerful discriminative capacity. There are many numerical characterizations of shape, and these can be used to provide components of feature vectors that are assigned to the objects studied. In this way, the comparison of the objects can be done in the feature vector space, i.e. in \mathbb{R}^n space, rather than in the object space. Working in \mathbb{R}^n is convenient for analysis as it is fast, and straightforward due to the available theoretical frameworks already developed. Because of this, shape based tools are intensively used in a wide spectrum of applications such as astrophysics [23], ecology [35], [5], materials analysis [26], medicine [15], politics [7], psychology [4], nano-technology [21], and many others.

In particular, the use of shape is widely used in content-based image retrieval systems. Sometimes it is combined with other features, e.g. shape and color together form “a powerful combination” [36]. However, for many applications their nature dictates that shape alone is used. For instance, for the retrieval of trademarks the cues like colour and texture are typically not relevant, and so query is performed using just shape retrieval [19].

Shape retrieval is also widely applied to 3D objects, which often do not contain colour information and therefore rely on geometry. Early methods used global features such as moments, spherical harmonics and shape distri-

butions [39] while subsequent techniques developed techniques that could cope better with geometric deformations of the objects. Most recently, deep learning has been deployed to discover shape descriptors [44].



Fig. 1. Some random shapes; these are intuitively judged as shapes whose circularity, elongation and convexity differ.

In the literature, shape descriptors tend to be either local or global, and our proposed method falls into the latter category. Although individual global descriptors may not be strong, they have the advantage that simpler matching schemes can be used than for matching local descriptors, and standard classifiers can be directly used without modification. Furthermore, combinations of multiple global descriptors enables strong classification and recognition levels.

Shape properties, like circularity, elongation, convexity, linearity, etc., have an intuitively clear meaning. For example, people would generally agree that the first shape in Fig.1 is the most circular of the shapes displayed, independently of which circularity measure is applied. Likewise, the second and third shapes are the most elongated and least convex shapes respectively. However, there are not many shape descriptors which have such an intuitively clear meaning. Consequently, this limited number of shape measures also limits the dimensionality of the corresponding feature vector spaces. We note also that several shape measures can be optimised by the same shapes, e.g. both linearity and elongation are optimised by a straight line.

- J. Žunić is with the Mathematical Institute, Serbian Academy of Sciences, Belgrade, Serbia.
E-mail: jovisa_zunic@mi.sanu.ac.rs
- P.L. Rosin is with the School of Computer Science and Informatics, Cardiff University, U.K.
E-mail: RosinPL@cardiff.ac.uk

The available alternative is to use generic shape measures, such as moments and Fourier descriptors. Although they do not provide intuitively clear behavior, they can provide an unbounded number of measures, enabling an arbitrarily large dimensional feature space to be provided.

In this paper we introduce a new family of shape measures that capture the benefits of both the above categories of approaches. The contributions of this paper are:

- A family of shape measures is introduced that consists of infinitely many measures, each of which is determined by a convex polygon.
- A tuning parameter (a real number) enables further control of the proposed shape measures.
- The new measures have predictable behavior and are intuitively interpretable.
- A family of convexity measures is obtained.

The paper is organized as follows. After discussion of related work in Section 2, the basic definitions and notations are given in Section 3. The main result is in Section 4, where the new family of the shape measures has been introduced. Experimental illustrations are in Section 5. The new family of convexity measures is considered in Section 6. Experiments on a known data set are in Section 7. Concluding remarks are in Section 8.

2 RELATED WORK

Many shape descriptors have been developed for characterising specific types of common shapes. Among them, some very popular ones are circularity [22], [28], [46], ellipticity [1], [20], [42], [48], linearity [14], [38], convexity [30], [32], [47], etc. For a given shape property, its alternative shape descriptors will vary according to robustness, computational efficiency, generalisability to higher dimensions, etc. Another significant variation is that although they should all characterise the ideal shape identically (i.e. the ideal shape should optimise the shape descriptor) they will characterise deviations from the ideal shape differently – see Fig.2.

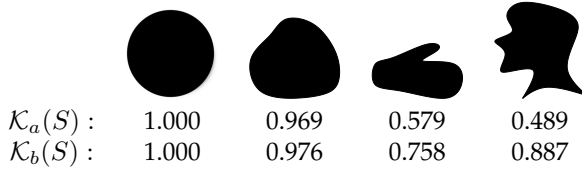


Fig. 2. Different circularity measures tend to rank shapes differently.

For example, a method to measure a shape's circularity can be derived by exploiting the following property of circular shapes:

- (a) *Among all the shapes having the same perimeter, the circle has the largest area.*¹

This approach leads to the following popular formula for computing circularity measure $K_a(S)$ of a given shape S :

$$K_a(S) = \frac{4 \cdot \pi \cdot \text{Area_of_}S}{(\text{Perimeter_of_}S)^2} \quad (1)$$

1. This solves Dido's famous problem [41].

Another geometric property that can be considered is:

- (b) *Among all the shapes having the same area, the circle has the smallest average square distance between the shape's points and shape centroid.*

which leads to a different, but also natural, way to define a circularity measure:

$$K_b(S) = \frac{1}{2\pi} \cdot \frac{\mu_{0,0}(S)^2}{\mu_{2,0}(S) + \mu_{0,2}(S)}, \quad (2)$$

where the quantities $\mu_{p,q}(S)$ are the *geometric moments*, defined as $\mu_{p,q}(S) = \iint_S x^p y^q dx dy$, under the presumption that the centroid of S and the origin coincide [37].

We note that in addition to the tendency of the two circularity measures to rank non-circular shapes differently (see Fig.2), we can also say that, due to its reliance on estimating the perimeter of a digitised shape, $K_a(S)$ will be more sensitive to discretisation artifacts and minor boundary fluctuations (e.g. roughness) than $K_b(S)$.

For the category of generic shape measures, one of the most popular approaches is to use moments; depending on the different polynomial bases selected, different polynomial bases can be chosen, leading to a range of types of moments [13], e.g. standard geometric, Zernike, Tchebichef, Legendre, etc. The usual requirement for shape measures is that they should be invariant w.r.t. at least rotation, translation and scaling transformations; and possibly further transformations such as affine or projection. Therefore, the raw moments must typically be normalised to provide such measures, e.g. the Hu moment invariants [17]. Although, theoretically, arbitrarily high order moments can be computed, in practice this is limited both by the available numerical precision as well as the sensitivity of higher order moments to noise [40], and the sensitivity of the various moments to noise is an ongoing research topic [11]. As we previously stated, such methods do not provide intuitively clear behavior. This is illustrated by the Hu moment invariants; although they have been intensively used and studied for more than 50 years it is only recently [46], [48] that the behavior of the first two Hu moment invariants was discovered, namely that the quantity in (2) is maximized by a circle (and is consequently a circularity measure) and that

$$\mathcal{P}(S) = \mu_{2,0}(S) \cdot \mu_{0,2}(S) - \mu_{1,1}(S)^2 \quad (3)$$

is minimized by ellipses (providing an ellipticity measure).

3 DEFINITIONS AND DENOTATIONS

In this section we give the basic definitions and notations which will be used throughout the paper.

- By a *shape* we mean a basic object property, that does not require a formal definition. A given planar shape is represented by a bounded region, in xy -plane, i.e. by the corresponding black and white image.
- $\text{line}(A, B)$ will denote the line passing through the points A and B ($A \neq B$). Similarly, the line determined by a given edge e will be denoted by $\text{line}(e)$.
- Let two points A and B ($A \neq B$) be given such that $\text{line}(A, B)$ does not include the origin $(0, 0)$.

H-plane(A, B) will denote the closed half-plane, determined by **line**(A, B), which includes $(0, 0)$. Similarly, **H-plane**(e) will denote the closed half-plane, determined by **line**(e), which includes the origin $(0, 0)$, provided that **line**(e) does not include the origin.

- $\text{Area}(S)$ denotes the area of a given planar shape S .
- \mathbb{R} denotes the set of real numbers.
- The centroid (or gravity center) of a planar shape S is $\left(\frac{\iint_S x \, dx \, dy}{\iint_S dx \, dy}, \frac{\iint_S y \, dx \, dy}{\iint_S dx \, dy} \right)$, and is the point whose coordinates are the average value of the coordinates of all the shape points.
- $\text{conv}(S)$ denotes the convex hull of a given shape S .
- By a *convex polygon* we will assume a convex planar region, bounded by a closed convex poly-line.
- We will assume that all appearing shapes have a strict positive area.
- Since we deal with area based shape descriptors (all the shape points are observed, not only the boundary ones), we will assume that two regions, whose set differences have area equal to zero have an equal shape. For example, we will say that the open circular disc $\{(x, y) \mid x^2 + y^2 < 1\}$ and the closed one $\{(x, y) \mid x^2 + y^2 \leq 1\}$ have the same shape. In this way we will avoid the need to discuss pathological situations and will make our proofs simpler. Of course, such an assumption is not a restriction in image processing and computer vision tasks, where we deal with real objects and their shapes.

4 MAIN RESULT

In this section we derive the main result of the paper. This result gives theoretical foundations for the definition of the shape measures introduced here. First, we define functions necessary for a formulation of the basic statements.

Definition 1. Let an edge e , whose end points are $A = (x_1, y_1)$ and $B = (x_2, y_2)$ ($A \neq B$), be given (i.e. $e = [AB] = [(x_1, y_1), (x_2, y_2)]$). Let the origin $(0, 0)$ not belong to **line**(e) (the line determined by A and B). The function $\psi_e(x, y)$ is defined as follows,

$$\psi_e(x, y) = \frac{y_2 - y_1}{x_1 \cdot y_2 - x_2 \cdot y_1} \cdot x + \frac{x_1 - x_2}{x_1 \cdot y_2 - x_2 \cdot y_1} \cdot y. \quad (4)$$

The function $\psi_e(x, y) = \psi_{[AB]}(x, y)$, as introduced in the previous definition, has the following properties:

$$\left. \begin{aligned} (i) \quad & \psi_e(x, y) \text{ is defined for all } x, y \in \mathbb{R}; \\ (ii) \quad & \psi_{[AB]}(x, y) = \psi_{[BA]}(x, y) \text{ for all } x, y \in \mathbb{R}; \\ (iii) \quad & \psi_e(x_1, y_1) = \psi_e(x_2, y_2) = 1; \\ (iv) \quad & \psi_e(x, y) = 1 \text{ for all } (x, y) \in \text{line}(e); \\ (v) \quad & \psi_e(x, y) \leq 1 \Leftrightarrow (x, y) \in \mathbf{H-plane}(e). \end{aligned} \right\} \quad (5)$$

The first property in (5) follows from the assumption that the origin is not collinear with A and B – this implies $x_1 \cdot y_2 - x_2 \cdot y_1 \neq 0$. The second, third and fourth properties in (5) are easy to verify. The fourth property, together with a trivial $\psi_e(0, 0) = 0$ proves the fifth property in (5).

Definition 2. Let a convex N -gon \mathbf{P} , whose centroid coincides with the origin, and a positive number λ , be given. Let e_1, e_2, \dots, e_N be edges of \mathbf{P} . We define the function $\Psi_{\lambda, \mathbf{P}}(x, y)$ as follows:

$$\Psi_{\lambda, \mathbf{P}}(x, y) = \max\{\psi_{e_1}(x, y), \dots, \psi_{e_N}(x, y)\}^\lambda. \quad (6)$$

Note 1. Since the polygon \mathbf{P} has a non-zero area and is convex, the centroid of \mathbf{P} does not belong to any line determined by the edges of \mathbf{P} . So, the functions $\psi_{e_1}(x, y), \psi_{e_2}(x, y), \dots, \psi_{e_N}(x, y)$, are defined for all $x, y \in \mathbb{R}$, (see (i) in (5)). This further implies that for any convex polygon \mathbf{P} , whose centroid coincides with the origin, the corresponding function $\Psi_{\lambda, \mathbf{P}}(x, y)$ is also defined for all $x, y \in \mathbb{R}$.

The next theorem proves a nice property of $\Psi_{\lambda, \mathbf{P}}(x, y)$. This property offers the basic arguments for the definition of the new family of shape measures, introduced later on.

Theorem 1. Let a convex N -gon \mathbf{P} , whose area is strictly positive and whose centroid coincides with the origin, and a real number $\lambda > 0$ be given. Let e_1, e_2, \dots, e_N be edges of \mathbf{P} . The function $\Psi_{\lambda, \mathbf{P}}(x, y)$, defined as in (6), has the following property:

$$\Psi_{\lambda, \mathbf{P}}(x, y) \leq 1 \Leftrightarrow (x, y) \in \mathbf{P}. \quad (7)$$

$$\Psi_{\lambda, \mathbf{P}}(x, y) \geq 0 \text{ for all } (x, y) \in \mathbf{P}. \quad (8)$$

Proof. In accordance with Note 1, all functions $\psi_{e_1}(x, y), \psi_{e_2}(x, y), \dots, \psi_{e_N}(x, y)$ are defined for all $x, y \in \mathbb{R}$, meaning that $\Psi_{\lambda, \mathbf{P}}(x, y)$ is also defined for all $x, y \in \mathbb{R}$.

Further, the property (v) in (5) gives:

$$\psi_{e_i}(x, y) \leq 1 \Leftrightarrow (x, y) \in \mathbf{H-plane}(e_i), \text{ for } 1 \leq i \leq N. \quad (9)$$

Taking into account (9) and the following identity

$$\mathbf{P} = \bigcap_{1 \leq i \leq N} \mathbf{H-plane}(e_i) \quad (10)$$

we deduce the required

$$\Psi_{\lambda, \mathbf{P}}(x, y) = \max_{1 \leq i \leq N} \{\psi_{e_i}(x, y)\}^\lambda \leq 1 \Leftrightarrow (x, y) \in \mathbf{P}.$$

Indeed, the implication: $(x, y) \in \mathbf{P} \Rightarrow \Psi_{\lambda, \mathbf{P}}(x, y) \leq 1$, is an immediate consequence of (10), (9) and (6). The implication $\Psi_{\lambda, \mathbf{P}}(x, y) \leq 1 \Rightarrow (x, y) \in \mathbf{P}$ can be proven by a contradiction. E.g. if $(x, y) \notin \mathbf{P}$ is assumed then, because of (10), there would exist a number $k \in \{1, \dots, N\}$ such that $(x, y) \notin \mathbf{H-plane}(e_k)$, which further would imply $\psi_{e_k}(x, y) > 1$. The last inequality would contradict the assumed $\Psi_{\lambda, \mathbf{P}}(x, y) \leq 1$.

To prove the inequality in (8) it is enough to notice that for any selected point $(x_0, y_0) \in \mathbf{P}$, there is an edge $e_i = [A_i B_i]$, of \mathbf{P} , ($1 \leq i \leq N$) such that the point (x, y) is inside the triangle whose vertices are the points A_i, B_i , and the origin $(0, 0)$. Since $\psi_{[A_i B_i]}(0, 0) = 0$ and $\psi_{[A_i B_i]}(x, y) = 1$, for any point (x, y) belonging to the edge $A_i B_i$, and since $\psi_{[a, b]}(x, y)$ is a monotonic function, with respect to its variables x and y , we deduce that $\psi_{[A_i B_i]}(x, y) \in [0, 1]$. Thus, $\psi_{[A_i B_i]}(x_0, y_0) \geq 0$.

This establishes the proof. \square

Now, we are ready to derive the main result of the paper.

Theorem 2. Let a shape S be given. Also, fix a convex polygon \mathbf{P} and a positive number λ . If the centroid of \mathbf{P} and the centroid of S are both coincident with the origin and if the area of S and the area of \mathbf{P} are the same, then the following two statements hold:

- (a) $\iint_S \Psi_{\lambda,\mathbf{P}}(x, y) dx dy = \iint_{\mathbf{P}} \Psi_{\lambda,\mathbf{P}}(x, y) dx dy$
 \Rightarrow shapes S and \mathbf{P} are equal.
- (b) If $S(\alpha)$ denotes the shape S rotated around the origin by angle α then

$$\min_{\alpha \in [0, 2\pi]} \iint_{S(\alpha)} \Psi_{\lambda,\mathbf{P}}(x, y) dx dy = \iint_{\mathbf{P}} \Psi_{\lambda,\mathbf{P}}(x, y) dx dy$$

$$\Leftrightarrow \text{shapes } S \text{ and } \mathbf{P} \text{ are equal.}$$

Proof. Let a shape S be given. Fix a parameter $\lambda > 0$ and a convex polygon \mathbf{P} , such that $\text{Area}(S) = \text{Area}(\mathbf{P})$. Let the centroid of S , the centroid of \mathbf{P} , and the origin coincide.

(a) We prove this by a contradiction. Let us assume that the shapes S and \mathbf{P} are different, i.e.

$$\text{Area}(S \setminus \mathbf{P}) = \text{Area}(\mathbf{P} \setminus S) > 0. \quad (11)$$

We will show that

$$\iint_S \Psi_{\lambda,\mathbf{P}}(x, y) dx dy = \iint_{\mathbf{P}} \Psi_{\lambda,\mathbf{P}}(x, y) dx dy \quad (12)$$

would lead to a contradiction, as follows.

Since all the points (x, y) satisfying $\Psi_{\lambda,\mathbf{P}}(x, y) \leq 1$ are inside the polygon \mathbf{P} (see (7)), and since $\Psi_{\lambda,\mathbf{P}}(x, y)$ is a continuous and non-constant function, inside the domain $\mathbf{P} \setminus S$, whose area is strictly positive (see the last item in Section 3), we deduce the following strict inequality

$$\iint_{\mathbf{P} \setminus S} \Psi_{\lambda,\mathbf{P}}(x, y) dx dy < \iint_{\mathbf{P} \setminus S} dx dy = \text{Area}(S \setminus \mathbf{P}). \quad (13)$$

Also, $(x, y) \in S \setminus \mathbf{P}$ implies $\Psi_{\lambda,\mathbf{P}}(x, y) \geq 1$ and further

$$\iint_{S \setminus \mathbf{P}} \Psi_{\lambda,\mathbf{P}}(x, y) dx dy \geq \iint_{S \setminus \mathbf{P}} dx dy = \text{Area}(S \setminus \mathbf{P}). \quad (14)$$

The inequalities in (13) and (14) give:

$$\iint_{\mathbf{P} \setminus S} \Psi_{\lambda,\mathbf{P}}(x, y) dx dy < \iint_{S \setminus \mathbf{P}} \Psi_{\lambda,\mathbf{P}}(x, y) dx dy.$$

The last strict inequality, together with a trivial equality:

$$\iint_{\mathbf{P} \cap S} \Psi_{\lambda,\mathbf{P}}(x, y) dx dy = \iint_{S \cap \mathbf{P}} \Psi_{\lambda,\mathbf{P}}(x, y) dx dy$$

contradicts with the equality assumed in (12). This proves item (a).

(b) This item follows from item (a), which actually says that $\iint_{S(\alpha)} \Psi_{\lambda,\mathbf{P}}(x, y) dx dy$ reaches the minimum possible value $\iint_{\mathbf{P}} \Psi_{\lambda,\mathbf{P}}(x, y) dx dy$ if and only if there is an angle α such that $S(\alpha) = \mathbf{P}$. \square

By the arguments of Theorem 2 we define a family of shape measures, $\mathcal{G}_{\lambda,\mathbf{P}}(S)$, where \mathbf{P} varies through the set of convex polygons, and λ varies through the set of positive

real numbers. Each of the new measures $\mathcal{G}_{\lambda,\mathbf{P}}(S)$ should evaluate how much the considered shape S looks like the preselected polygon \mathbf{P} . Since the scaling transformation does not change the object shape, we will assume that the polygon \mathbf{P} and the shape S both have area equal to 1.

Definition 3. Let \mathbf{P} be a convex polygon scaled to have its area equal to 1 and placed so that its centroid coincides with the origin, and let a positive number λ be given. For a short notation we write

$$C_{\lambda,\mathbf{P}} = \iint_{\mathbf{P}} \Psi_{\lambda,\mathbf{P}}(x, y) dx dy. \quad (15)$$

Let a given shape S also be scaled to have its area equal to 1 and placed so that its centroid coincides with the origin.

The shape measure $\mathcal{G}_{\lambda,\mathbf{P}}(S)$ of S is defined as

$$\mathcal{G}_{\lambda,\mathbf{P}}(S) = C_{\lambda,\mathbf{P}} \cdot \frac{1}{\min_{\alpha \in [0, 2\pi]} \iint_{S(\alpha)} \Psi_{\lambda,\mathbf{P}}(x, y) dx dy} \quad (16)$$

where $\Psi_{\lambda,\mathbf{P}}(x, y)$ is defined as in (6) and $S(\alpha)$ denotes the shape S rotated around the origin by angle α .

Now, we summarize the desirable properties of $\mathcal{G}_{\lambda,\mathbf{P}}(S)$.

Theorem 3. Fix a convex polygon \mathbf{P} and a $\lambda > 0$. All the shape measures $\mathcal{G}_{\lambda,\mathbf{P}}(S)$ have the following properties:

- (a) $\mathcal{G}_{\lambda,\mathbf{P}}(S) \in (0, 1]$, for all the shapes S ;
- (b) $\mathcal{G}_{\lambda,\mathbf{P}}(S) = 1$ if and only if the shapes S and \mathbf{P} are equal;
- (c) $\mathcal{G}_{\lambda,\mathbf{P}}(S)$ is invariant with respect to translation, rotation and scaling transformations.

Proof. Theorems 1 and 2 give (a) and (b). To prove (c): $\mathcal{G}_{\lambda,\mathbf{P}}(S)$ is translation and rotation invariant by the definition. Since the method applies a size normalisation step before computation of $\mathcal{G}_{\lambda,\mathbf{P}}$ in order to eliminate the effect of scaling, it therefore follows that $\mathcal{G}_{\lambda,\mathbf{P}}(r \cdot S) = \mathcal{G}_{\lambda,\mathbf{P}}(S)$ is true for all $r > 0$, with $r \cdot S = \{(r \cdot x, r \cdot y) \mid (x, y) \in S\}$. \square

At the end of this section we now comment and give experimental illustration related to the cost of the computation of $\mathcal{G}_{\lambda,\mathbf{P}}(S)$ and to an analysis of the function $\Psi_{\lambda,\mathbf{P}}(x, y)$, crucial in the definition of $\mathcal{G}_{\lambda,\mathbf{P}}(S)$.

Computation cost of the new measure. In practical implementations of the methods for the computation of the measures involved, we have to work with digital images and to estimate the values $\mathcal{G}_{\lambda,\mathbf{P}}(S)$ numerically. Since the considered shape S is given by the set of pixels, the integral is estimated by a sum as follows

$$\iint_{S(\alpha)} \Psi_{\lambda,\mathbf{P}}(x, y) dx dy \approx \sum_{(i(\alpha), j(\alpha)) \in S(\alpha)} \Psi_{\lambda,\mathbf{P}}(i(\alpha), j(\alpha)) \quad (17)$$

where $(i(\alpha), j(\alpha))$ are coordinates of the pixel $(i, j) \in S$ after being rotated by angle α . The minimal value $\min_{\alpha \in [0, 2\pi]} \iint_{S(\alpha)} \Psi_{\lambda,\mathbf{P}}(x, y) dx dy$ is estimated by repeating the computation in (17) for an incremental increase $(\Delta\alpha)$ of the angle α , within the interval $[0, 2\pi)$. The computation in (17) depends on the number of pixels inside S (i.e. on the resolution of image of S) and the number of edges of the reference polygon \mathbf{P} (see (2)). More formally, the computation complexity can be estimated as $\mathcal{O}(r \cdot N \cdot (2\pi/\Delta))$,

where: r denotes the number of pixels per unit (in the shape image used); N equals the number of sides of the reference polygon used; Δ is the angle increment used for the numerical computation. Due to the fact that the integral approximated in (17) is an area integral and that the sub-integral function $\Psi_{\lambda, \mathbf{P}}(x, y)$ is continuous, the approximation in (17) is efficient. This is a nice and well known property [8], [18].² The property implies that both the angle increment (difference between two consecutive values of α used) and the resolution of image of S do not need to be high. This is illustrated by the example in Fig.3. In the first row, on the left, is the reference polygon \mathbf{P} . The original kangaroo shape is the second shape in the first row.

–The values in the table below the images illustrate that the estimated values of $\mathcal{G}_{\lambda=1, \mathbf{P}}$ converge quickly even for relatively small increment values of α (e.g. $\Delta\alpha = \pi/64$). In all the diatom classification experiments (Section 7) we use $\Delta\alpha = \pi/256$.

– The values in the bottom table in Fig.3 illustrate that the relatively low resolution of image of S enables an efficient approximation. Indeed, $\mathcal{G}_{\lambda=1, \mathbf{P}}(S) \approx 0.810983$ is obtained for the kangaroo image displayed next to the reference polygon, at the top in Fig.3. But two, four, and even eight times lower resolution (3rd shape in the first row), of the image of S , give a similar approximation of $\mathcal{G}_{\lambda=1, \mathbf{P}}(S)$. Of course, further decrease in resolution (of the image of S) leads to greater deformation of the original shape and subsequently greater differences in the computed $\mathcal{G}_{\lambda=1, \mathbf{P}}(S)$ values. For sixteen times reduction in resolution (the last shape in the first row) we have $\mathcal{G}_{\lambda=1, \mathbf{P}}(S) = 0.844234$ and for thirty two times reduction $\mathcal{G}_{\lambda=1, \mathbf{P}}(S) = 0.919404$.

Meaning of $\Psi_{\lambda, \mathbf{P}}(x, y)$ function. Here we illustrate the behavior of the function $\Psi_{\lambda, \mathbf{P}}(x, y)$. The same convex 7-gon \mathbf{P} (displayed in the third column in Fig.4) is used to define functions $\Psi_{\lambda=1, \mathbf{P}}(x, y)$ and $\Psi_{\lambda=5, \mathbf{P}}(x, y)$. The corresponding images/plots of these functions are given in the first two columns in Fig.4. The plots of the functions $\Psi_{\lambda=1, \mathbf{P}}(x, y)$ and $\Psi_{\lambda=5, \mathbf{P}}(x, y)$ are given separately for $(x, y) \in \mathbf{P}$ (images in the top row) and for $(x, y) \notin \mathbf{P}$ (images in the second row). This has been done to improve the visualization. In the first row, the interior points of the 7-gon polygon \mathbf{P} represent the $\Psi_{\lambda=1, \mathbf{P}}(x, y)$ and $\Psi_{\lambda=5, \mathbf{P}}(x, y)$ values according to the assigned gray values. The centroid of \mathbf{P} is represented by a black pixel, in both of these sub-figures. This is in accordance with $\Psi_{\lambda, \mathbf{P}}(0, 0) = 0$, for all λ . This follows from the definition of $\Psi_{\lambda, \mathbf{P}}(x, y)$ and the assumption that the origin $(0, 0)$ and centroid of \mathbf{P} coincide. The value of $\Psi_{\lambda, \mathbf{P}}(x, y)$ increases not only according to the distance of $(x, y) \in \mathbf{P}$ from the centroid of \mathbf{P} , but also depending on the position of (x, y) with respect to the edges of \mathbf{P} . At the points of the boundary of \mathbf{P} we have $\Psi_{\lambda, \mathbf{P}}(x, y) = 1$, for all λ . This is in accordance with (iv) in (5). It also can be said that the plot of $\Psi_{\lambda, \mathbf{P}}(x, y)$ is influenced by the shape of \mathbf{P} . Note that, for better visualization, in both sub-figures (on the left, in the top row), all the background pixels of \mathbf{P} are displayed as black.

The values of $\Psi_{\lambda, \mathbf{P}}(x, y)$ outside the polygon \mathbf{P} are illus-

trated by the sub-figures in the second row, for $\lambda = 1$ and $\lambda = 5$, respectively. Since $\Psi_{\lambda, \mathbf{P}}(x, y) > 1$, for $(x, y) \notin \mathbf{P}$, we normalize the $\Psi_{\lambda=1, \mathbf{P}}(x, y)$ and $\Psi_{\lambda=5, \mathbf{P}}(x, y)$ values to be in the range $[0, 1]$, for (x, y) inside the presented domain, again for visualization purposes. Similarly as in the case $(x, y) \in \mathbf{P}$, $\Psi_{\lambda, \mathbf{P}}(x, y)$ values depend on both distance of (x, y) from the centroid of \mathbf{P} and on the position of (x, y) with respect to the boundary edges of \mathbf{P} . Also, the plot of $\Psi_{\lambda, \mathbf{P}}(x, y)$, for $(x, y) \notin \mathbf{P}$, is dependent on the shape of \mathbf{P} . Note that in both sub-figures the points inside \mathbf{P} are displayed as white for better visualization.

If we compare the figures in the first column, corresponding to the $\Psi_{\lambda=1, \mathbf{P}}(x, y)$ function, against the figures in the second column, corresponding to $\Psi_{\lambda=5, \mathbf{P}}(x, y)$ we see the influence of the parameter λ to the behavior of $\Psi_{\lambda, \mathbf{P}}(x, y)$, as λ varies.

Note. Observing a known measure $IoU_{\mathbf{P}}(S)$, defined as in (20), we may say that this method gives the same weights, equal to 1, to the points inside \mathbf{P} , and the weights equal to 0, to all the points outside \mathbf{P} . This is obviously not the case if new points are applied, as illustrated by the plots in Fig.4.

Selection of the reference polygon. The choice of the best reference polygon for the shape measure will depend on the specific application of the measure. Here we outline some possible general strategies for selecting or generating reference polygons.

Let us assume that the shape measure should be applied to a dataset of shapes. First, we divide the types of reference polygons into two classes: those which are fixed for the whole dataset, and those which are adapted for each shape. For the former category, it is natural to use basic, general, convex geometric shapes: square, circle, rectangle, triangle, etc. Consequently, $\mathcal{G}_{\lambda, \mathbf{P}}(S)$ will provide measures analogous to classical shape measures of squareness, circularity, etc.

Another choice for a pan-dataset reference polygon is to generate a polygon reflecting the characteristics of the shapes in the data set, e.g. the mean shape's convex hull.

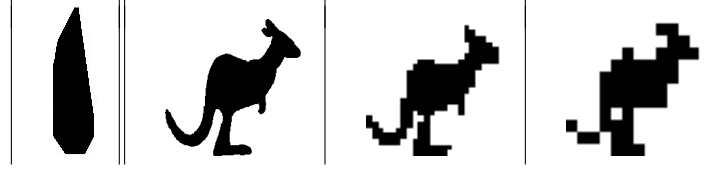
A third possibility is to determine reference polygons that optimise a cost function derived from the application, e.g. that maximise classification accuracy. Although such optimisation is likely to be computationally expensive, this step would be performed off-line using the training data.

Finally, for the latter category of reference polygons, which are adapted for each shape in the dataset, we can use various convex polygons that are fitted to each shape. Examples include the convex hull (see also Section 6), convex skull (i.e. maximum area inscribed convex hull), kernel, minimum bounding rectangle, etc.

5 EXPERIMENTAL ILLUSTRATIONS

In this section we provide some experimental illustration, based on synthetic, randomly selected shapes, in order to support a better understanding how the new shape measures behave. The experiments are divided into two subsections: The first one related to experiments with λ fixed and equal to 1. For a short denotation we will use $\mathcal{G}_{\mathbf{P}}(S)$ instead of $\mathcal{G}_{\lambda=1, \mathbf{P}}(S)$. In the second subsection we provide experiments where λ varies.

2. Note that such an efficient approximation does not exist if boundary integration (e.g. curve or surface integration) of noncontinuous functions would be used.



Estimated $\mathcal{G}_{\lambda=1, \mathbf{P}}(S)$ value (for the second shape in the row above), depending on the angle increment $\Delta\alpha$ used

angle increment	$\Delta\alpha = \pi/8$	$\Delta\alpha = \pi/16$	$\Delta\alpha = \pi/32$	$\Delta\alpha = \pi/64$	$\Delta\alpha = \pi/128$	$\Delta\alpha = \pi/256$	$\Delta\alpha = \pi/512$
$\mathcal{G}_{\lambda=1, \mathbf{P}} \approx$	0.791373	0.806383	0.809611	0.810759	0.810864	0.810983	0.810983

Estimated $\mathcal{G}_{\lambda=1, \mathbf{P}}$ value, depending on the applied image resolution

	original image	resolution / 2	resolution / 4	resolution / 8	resolution / 16	resolution / 32
$\mathcal{G}_{\lambda=1, \mathbf{P}} \approx$	0.810983	0.812875	0.817435	0.814804	0.844234	0.919404

Fig. 3. The reference polygon \mathbf{P} is on the left. The second, third, and fourth shapes correspond to a kangaroo image at an initial resolution, and 8 and 16 times lower resolution, respectively. The first table provides values of $\mathcal{G}_{\lambda=1, \mathbf{P}}(S)$ computed numerically for the full resolution image at different rotation angle increments. The second table shows $\mathcal{G}_{\lambda=1, \mathbf{P}}(S)$ values obtained for different image resolutions of the kangaroo shape.

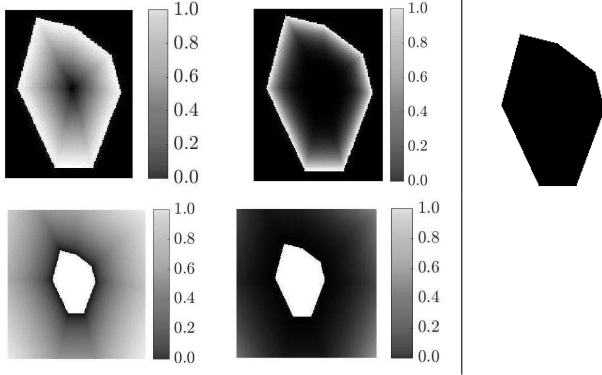


Fig. 4. First row: Two sub-figures on the left show the behavior of $\Psi_{\lambda=1, \mathbf{P}}(x, y)$ and $\Psi_{\lambda=5, \mathbf{P}}(x, y)$, respectively, for the points (x, y) inside the reference polygon \mathbf{P} (on the right). Second row: Sub-figures the behavior of $\Psi_{\lambda=1, \mathbf{P}}(x, y)$ and $\Psi_{\lambda=5, \mathbf{P}}(x, y)$ for $(x, y) \notin \mathbf{P}$.

5.1 Experiments Illustrating the $\mathcal{G}_{\lambda=1, \mathbf{P}}(S)$ Behavior

Three experiments are provided in this subsection. Since the measure $\mathcal{G}_{\mathbf{P}}(S)$ should express the degree to which a given shape S looks like the selected polygon \mathbf{P} , it could be said that the shapes, in each row, are ranked in accordance with this criterion. For example, in Fig.5 the human silhouette, next to the triangle in the first row, looks more similar to this triangle than the next two human silhouettes, in the same row. Also, all three the human shapes are more similar to the triangle (in the first row) than the last shape, in the same row, is. Thus, as expected, this shape has the lowest $\mathcal{G}_{\mathbf{P}}(S)$ value (equal to 0.4686) among all the measured shapes (in the first row). Similar comments might be given for the shapes in the remaining three rows.

It is important to point out that the ranking according to $\mathcal{G}_{\mathbf{P}}(S)$ strongly depends on the convex polygon \mathbf{P} . Indeed, the human silhouettes ranked first and second in the first row, have changed their order when the triangle in the first row is replaced by the triangle in the second row. Similarly, the human shapes in the first row, ranked first and third in the first row, swap their ranking if the triangle (in the first row) is replaced by the rectangle, on the left, in the third row.

The shapes in the fourth column are given to illustrate

the diversity of situations where $\mathcal{G}_{\mathbf{P}}(S)$ can be applied directly, without any modification needed. Indeed, the first shape, in the fourth column, has a hole, the last shape in the same column consists of many components, the second shape has both multiple components and holes, and so on.

Second experiment: $\mathcal{G}_{\mathbf{P}}(S)$ behavior in the case of the object deformations. To illustrate the behavior of $\mathcal{G}_{\mathbf{P}}(S)$ when the shapes deform, we have used three human silhouettes, displayed in Fig.6, and have measured them by $\mathcal{G}_{\mathbf{P}}(S)$, for three different choices of \mathbf{P} (displayed in the left column in Fig.6). The shape silhouettes used can be understood as the shapes of the same object, subjected to slight deformations.

Third experiment: Robustness of the $\mathcal{G}_{\mathbf{P}}(S)$ measure. In this experiment (see Fig.7) we illustrate the robustness of the $\mathcal{G}_{\mathbf{P}}(S)$ measure. More precisely, we consider the robustness with respect to the defects caused by added noise. Actually, the robustness property of $\mathcal{G}_{\mathbf{P}}(S)$ is expected. This is due to the fact that it is an area based measure – i.e. $\mathcal{G}_{\mathbf{P}}(S)$ uses all the shape points for the computation. It is worth mentioning that such robustness would not be expected if the computation is based on the shape boundary points only, some curvature based features, etc. Four circular shapes and four polygonal shapes affected by noise were used. The circular shapes are in the first row in Fig.7. The first two circle shapes are affected by ‘salt’ noise while the third and fourth circular shape are affected by noise added to the circle boundary. The results illustrate that even a big change in the level of noise added does not lead to a big change in the computed $\mathcal{G}_{\mathbf{P}}(S)$ values: between the first and second circular shape; and between third and fourth circular shape. The computed $\mathcal{G}_{\mathbf{P}}(S)$ values are in Fig.7, below the related shapes. This is in accordance with our expectation that the $\mathcal{G}_{\mathbf{P}}(S)$ measure is robust. Also, we notice that the measure $\mathcal{G}_{\mathbf{P}}(S)$ is more sensitive to the defects inside the shape than to defects on the shape boundary. Similar comments can be given for the results related to the shapes in the second row in Fig.7. The first polygonal shape $S5$, in the second row, is a noise free shape, while the remaining three shapes ($S6$, $S7$, and $S8$) are with a different noise level added, to the shape boundaries. Deformations on the shape





















Shape P	Ranked first	Ranked second	Ranked third	Ranked fourth
	 $\mathcal{G}_P = 0.9042$	 $\mathcal{G}_P = 0.8531$	 $\mathcal{G}_P = 0.8515$	 $\mathcal{G}_P = 0.4686$
	 $\mathcal{G}_P = 0.8021$	 $\mathcal{G}_P = 0.7570$	 $\mathcal{G}_P = 0.3752$	 $\mathcal{G}_P = 0.3181$
	 $\mathcal{G}_P = 0.8774$	 $\mathcal{G}_P = 0.8380$	 $\mathcal{G}_P = 0.6886$	 $\mathcal{G}_P = 0.3034$
	 $\mathcal{G}_P = 0.9232$	 $\mathcal{G}_P = 0.8622$	 $\mathcal{G}_P = 0.5726$	 $\mathcal{G}_P = 0.2509$

Fig. 5. In all the rows, the polygon on the left is used to define the $\mathcal{G}_P(S)$ measure. The remaining 4 shapes (in each row) are listed in accordance with their decreasing $\mathcal{G}_P(S)$ value. The computed $\mathcal{G}_P(S)$ values are given next to their corresponded shapes.













Shapes \rightarrow P \downarrow	Ranked 1st	Ranked 2nd	Ranked 3rd
	 $\mathcal{G}_P = 0.8694$	 $\mathcal{G}_P = 0.8577$	 $\mathcal{G}_P = 0.8508$
(a)			
	 $\mathcal{G}_P = 0.9112$	 $\mathcal{G}_P = 0.8663$	 $\mathcal{G}_P = 0.8528$
(b)			
	 $\mathcal{G}_P = 0.8954$	 $\mathcal{G}_P = 0.8603$	 $\mathcal{G}_P = 0.8558$
(c)			

Fig. 6. Three shapes, ranked by $\mathcal{G}_P(S)$ measure (for different choices of the polygon P) are in the first row. The selected polygons, used for the computation of $\mathcal{G}_P(S)$, are displayed on the left, in the rows (a), (b), and (c). The shapes observed are displayed in the second, third, and fourth row, according to their computed $\mathcal{G}_P(S)$ values.

boundary, caused by the added noise, do not much affect the computed $\mathcal{G}_P(S)$ values, even in the case of a high level of added noise (the shape S8). The values obtained are in Fig.7, below the shapes related.

5.2 Experiments Related to the Behavior of Tunable Shape Measures $\mathcal{G}_{\lambda,P}(S)$ and Further Analysis

In this subsection we provide experiments illustrating the behavior of $\mathcal{G}_{\lambda,P}(S)$, where λ varies.

Fourth Experiment: Behavior of the measures from the $\mathcal{G}_{\lambda,P}(S)$ family. The behavior of the measures $\mathcal{G}_{\lambda,P}(S)$ is illustrated by the experiments in Fig.8. Two $\mathcal{G}_{\lambda,P}(S)$ measures, determined by a choice of the polygons P1 and P2 (displayed in the left column in Fig.8), are observed. The graphs of $\mathcal{G}_{\lambda,P1}(S)$ and $\mathcal{G}_{\lambda,P2}(S)$, for λ varying through the interval $[0, 5]$, and for a choice of four diverse shapes S1, S2, S3, and S4, are displayed below those shapes. In accordance with the definition, $\mathcal{G}_{\lambda=0,P}(S) = 1$ is true for every choice of P and S. This is why all the graphs of $\mathcal{G}_{\lambda,P}(S)$ start at the point (0, 1). For $P \neq S$, the function (i.e. measure) $\mathcal{G}_{\lambda,P}(S)$ decreases as λ increases. It could be said: A bigger "difference" between the polygon P and the measured shape S leads to a faster decrease of $\mathcal{G}_{\lambda,P}(S)$. In Fig.8, the values of $\mathcal{G}_{\lambda,P}(S4)$ (the graphs in the right column) decrease fastest among the examples given. This might be expected since the shape S4 consists of many disconnected components and the "whole" shape does not look "similar" to the polygons P1 and P2. This property of $\mathcal{G}_{\lambda,P}(S)$ is a good one, since it makes possible to "tune" the importance of the dissimilarity (between P and S) impact to the computed $\mathcal{G}_{\lambda,P}(S)$ values, by a suitable choice of λ . This issue will be also discussed related to the experiments in Fig.10.

It is very important to mention that for suitable choices of the parameter λ , the measure $\mathcal{G}_{\lambda,P1}(S)$ could provide different shape ranking – e.g. for S1 and S2, we have:

- $\mathcal{G}_{\lambda=3.5,P1}(S1) < \mathcal{G}_{\lambda=3.5,P1}(S2)$;
- $\mathcal{G}_{\lambda=1.1,P1}(S1) > \mathcal{G}_{\lambda=1.1,P1}(S2)$.

The graphs of the difference and the ratio between the measures $\mathcal{G}_{\lambda,P1}(S1)$ and $\mathcal{G}_{\lambda,P1}(S2)$, for $\lambda \in (0, 5]$, are the

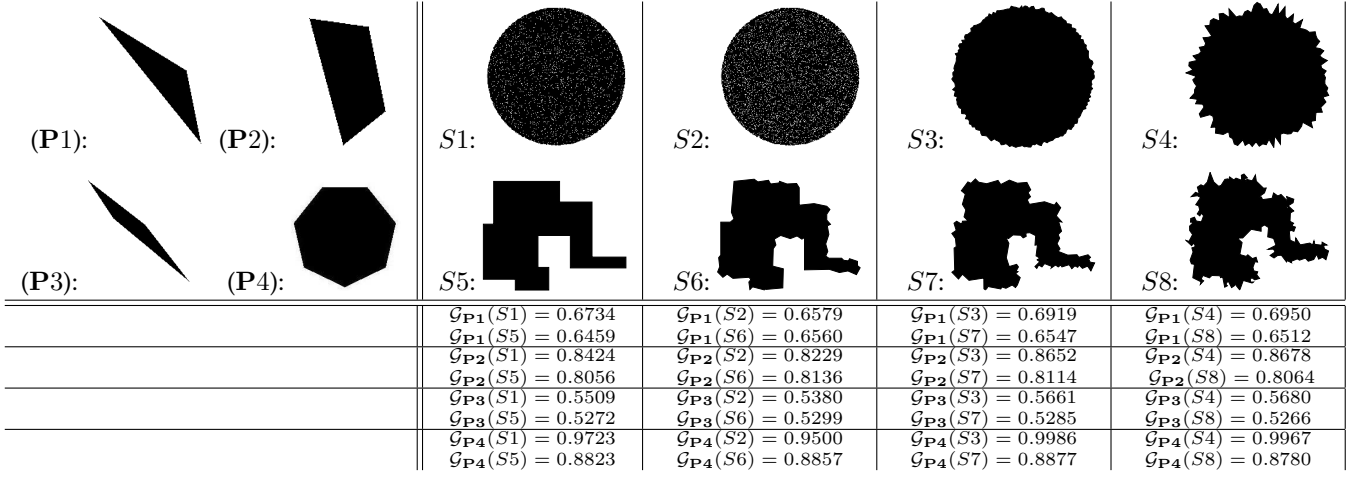


Fig. 7. $S1 - S4$ circle shapes, affected by noise, are in the first row. The polygonal shape $S5$, in the second row, is noise-free, while the remaining three shapes $S6 - S8$ are affected by noise. $\mathcal{G}_P(S)$ values, are below the corresponding shapes. $\mathcal{G}_P(S)$ values for a noise-free circle are 0.6909, 0.8645, 0.5652, and 0.9986, respectively, if the polygons $P1$, $P2$, $P3$, and $P4$ were used.

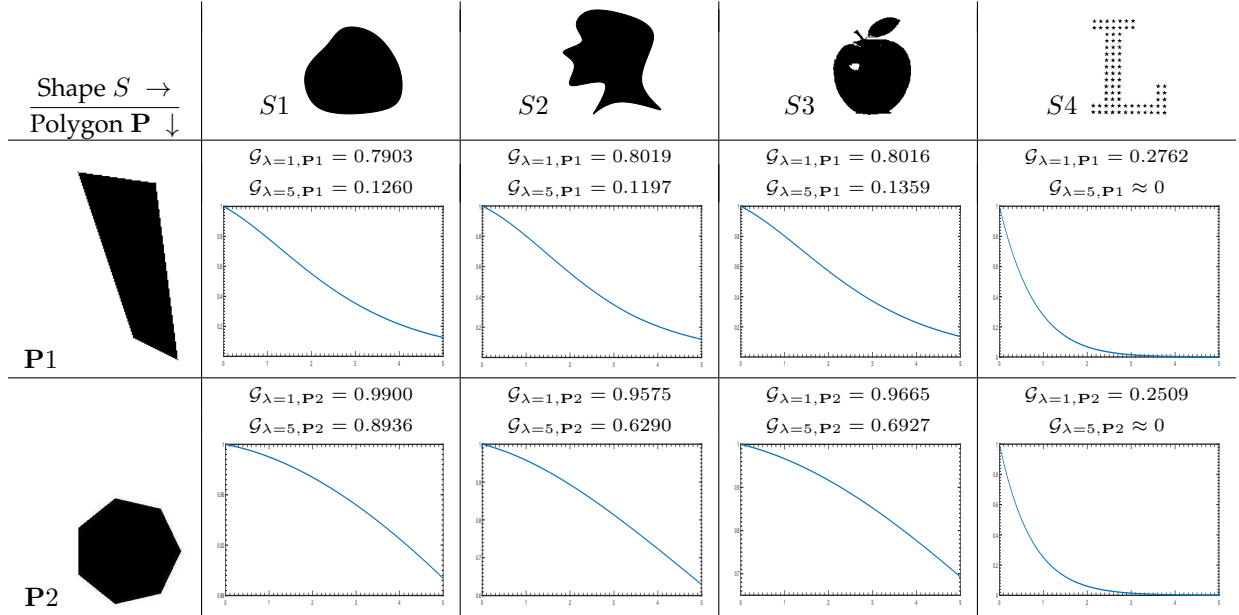


Fig. 8. Polygons $P1$ and $P2$ used to define $\mathcal{G}_{\lambda,P1}(S)$ and $\mathcal{G}_{\lambda,P2}(S)$ are in the left column. The shapes measured are in the top row. Their corresponded graphs $\mathcal{G}_{\lambda,P1}(S)$ and $\mathcal{G}_{\lambda,P2}(S)$ for $\lambda \in [0, 5]$, are below them. The values $\mathcal{G}_{\lambda=1,P1}(S)$ and $\mathcal{G}_{\lambda=5,P1}(S)$, are also included.

the two graphs on the left in Fig.9. Related to the shapes $S3$ and $S4$, the graphs of the difference and ratio of $\mathcal{G}_{\lambda,P1}(S3)$ and $\mathcal{G}_{\lambda,P1}(S4)$, for $\lambda \in [0, 5]$, are on the right (top row in Fig.9). It can be seen that the difference graphs, as well as the ratio graphs, differ essentially (in shape). This again illustrates the diversity of the measures $\mathcal{G}_{\lambda,P}(S)$. It is worth noticing that the difference $\mathcal{G}_{\lambda,P1}(S3) - \mathcal{G}_{\lambda,P1}(S4)$ is always positive, except for $\lambda = 0$ where the difference is equal to 0 as both measures take the value equal to 1. This can be explained by the fact that shape $S3$ and polygon $P1$ are more similar than $S4$ and polygon $P1$. This is even more visible if we consider the graph of the ratio of $\mathcal{G}_{\lambda,P1}(S3)$ and $\mathcal{G}_{\lambda,P1}(S4)$. The ratio monotonically increases as λ increases. Even for a relatively small $\lambda = 5$ this ratio becomes very high (equal to 222.66).

In the next two figures (Fig.10 and Fig.11), we consider

the robustness of $\mathcal{G}_{\lambda,P}(S)$ in the presence of noise. In the first row in Fig.10 a noise free rectangle is given. If we chose this triangle to play the role of the polygon P , the value of $\mathcal{G}_{\lambda,P}(P)$ would not depend on the parameter λ and would be always equal to 1. The second and third shapes, in the first row, in Fig.10, have a small level of noise added. The computed values of the measure $\mathcal{G}_{\lambda=1,P}(S)$ are 0.9961 and 0.9860. Since both values are very close to 1 it could cause an uncertainty as to whether the noise is really present, or whether the difference might be caused by the numerical calculation, for example. If $\lambda = 5$ is chosen, then the presence of noise becomes evident since $\mathcal{G}_{\lambda=5,P}(S) = 0.9571$ $\mathcal{G}_{\lambda=5,P}(S) = 0.8502$ differs more from the value of 1, corresponding to a noise free triangle P .

For a higher value of noise added (fourth shape) the presence of noise is evident for both $\lambda = 1$ and $\lambda = 5$. The

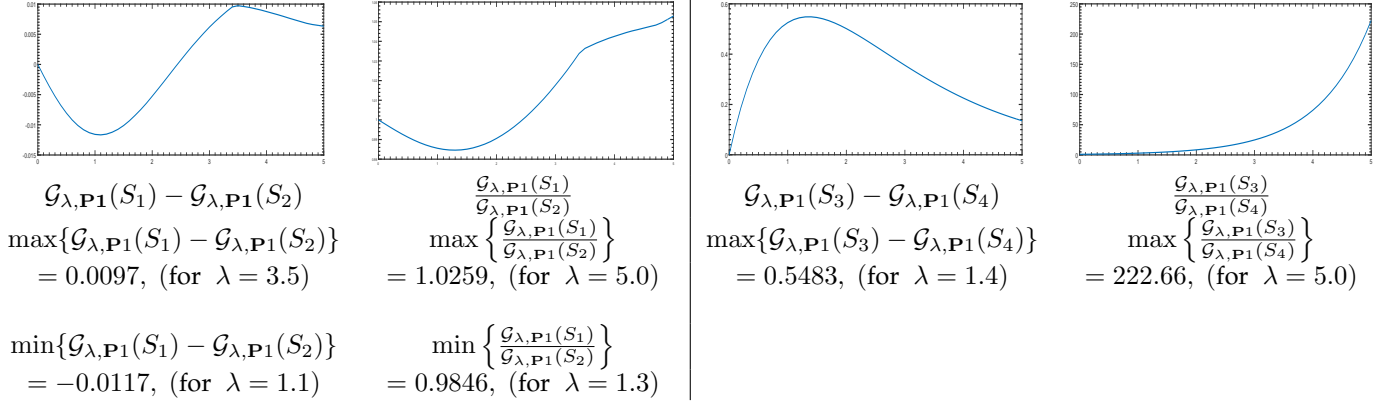


Fig. 9. The graphs of the difference and ratio of $\mathcal{G}_{\lambda, P_1}(S_1)$ and $\mathcal{G}_{\lambda, P_1}(S_2)$, for $\lambda \in [0, 5]$, are on the left. The related minimum and maximum values are also given. The related graphs for the shapes S_3 and S_4 , are third and fourth graph in the top row. In this case the difference minimum is 0 while the ratio minimum is equal to 1, both are reached for $\lambda = 0$.

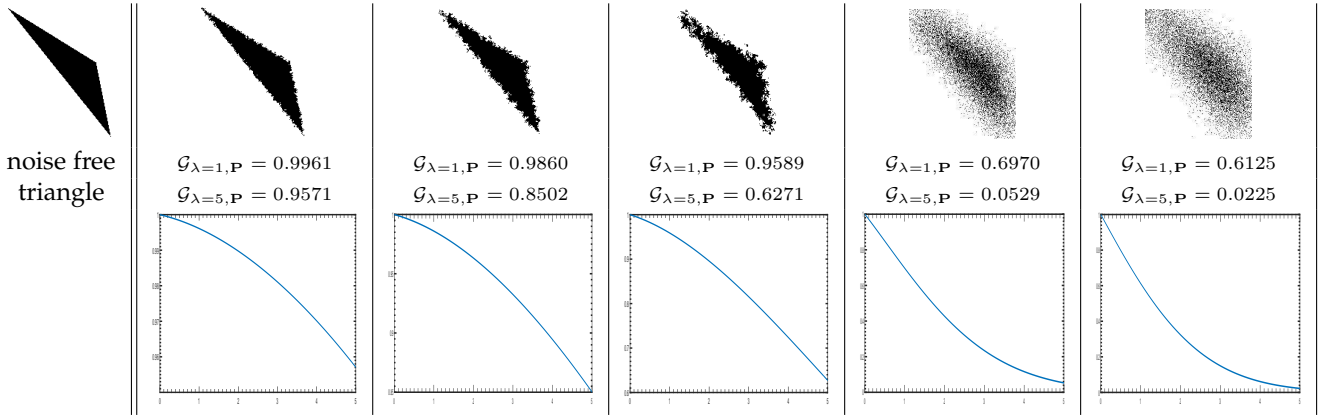


Fig. 10. A noise free triangle is on the left in the first row. The remaining five shapes correspond to the same triangle with added different levels of noise. The graphs of $\mathcal{G}_{\lambda, P}(S)$, $\lambda \in [0, 5]$, are below these shapes, as well as their computed values for $\lambda = 1$ and $\lambda = 5$.

graphs below the shapes show that the influence of noise on the computed measure can be increased by a selecting a larger λ , or reduced by selecting a smaller λ .

The fifth and sixth shapes have a very large amount of noise added, which further reduces the computed values from 1. In the case of the sixth shape with $\lambda = 5$, the computed measure almost vanishes. In the top row in Fig.11 there are two circular shapes affected by salt noise, and two circular shapes with noise added to their boundaries. Two polygons, P_1 and P_2 , in the column on the left, were used to define the measures $\mathcal{G}_{\lambda, P}(S)$. The polygon P_1 is a regular 7-gon. As such, this polygon is very similar to a perfect circle, and all the circularity measures would assign a very high circularity measure. Thus, a very high $\mathcal{G}_{\lambda=1, P_1}(S)$ value, close to 1, would be assigned to a perfect circle (notice that we do not know the exact value). As expected, very high $\mathcal{G}_{\lambda=1, P_1}(S)$ measures are assigned to the circles affected by noise. These values, for the shapes S_1 , S_2 , S_3 , and S_4 are 0.9723, 0.9500, 0.9986, and 0.9967, respectively (see Fig.7). Thus, the presence of noise in the case of shapes S_3 and S_4 cannot be clearly seen from the computed values of $\mathcal{G}_{\lambda=1, P_1}(S)$. To achieve a clear distinction between a noise free circle and perfect ones it would be enough to apply the measures $\mathcal{G}_{\lambda, P_1}(S)$ with λ substantially larger than 1. Indeed, the presence of noise, in all the shapes displayed

becomes evident if $\mathcal{G}_{\lambda=10, P_1}(S)$ is used. The computed values are in Fig.11, above the corresponding graphs of $\mathcal{G}_{\lambda, P_1}(S)$, $\lambda \in [0, 10]$.

If the polygon P_2 is used as a reference polygon, the computed values $\mathcal{G}_{\lambda, P_2}(S)$ are much smaller than if $\mathcal{G}_{\lambda, P_1}(S)$ would be applied. This is because P_2 does not "look" like a circle. Still, $\mathcal{G}_{\lambda, P_2}(S)$ can be evaluated robustly since even $\mathcal{G}_{\lambda=10, P_2}(S_1)$ and $\mathcal{G}_{\lambda=10, P_2}(S_2)$, or $\mathcal{G}_{\lambda=10, P_2}(S_3)$ and $\mathcal{G}_{\lambda=10, P_2}(S_4)$ do not differ too much, even though a relatively large $\lambda = 10$ was selected.

6 NEW FAMILY OF CONVEXITY MEASURES

In this section we define a new family $\mathcal{C}_\lambda(S)$ of convexity measures, as a subfamily of the family $\mathcal{G}_{\lambda, P}(S)$. More precisely, $\mathcal{C}_\lambda(S)$ equals $\mathcal{G}_{\lambda, P}(S)$, if the polygon P is chosen to be the convex hull ($\text{conv}(S)$) of S . In accordance with the definition, before applying the formula for the $\mathcal{G}_{\lambda, P}(S)$ computation, both $P = \text{conv}(S)$ and S have to be positioned such that their centroids coincide with the origin, and scaled so that their areas are equal to 1. The role of the parameter λ is to control the sensitivity/robustness of the measures from the family $\mathcal{C}_\lambda(S)$. Smaller λ values correspond to more robust measures, while bigger λ values correspond to more sensitive convexity measures.

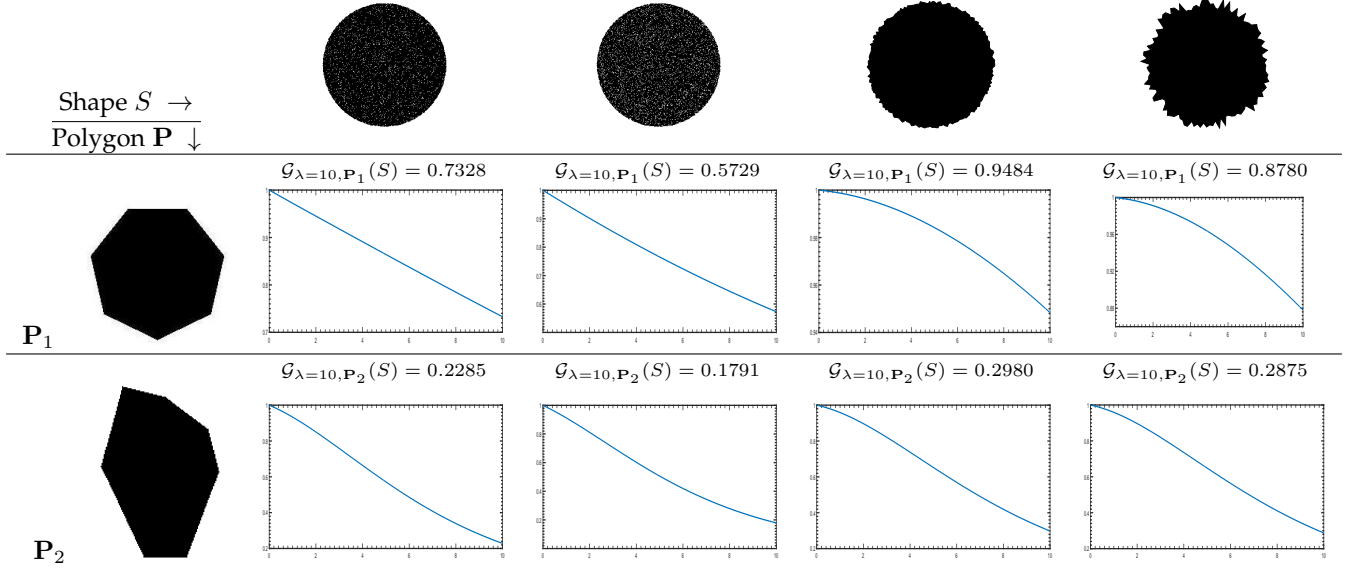


Fig. 11. Circular shapes, affected by noise, are in the top row. They are measured by $\mathcal{G}_{\lambda, P_1}(S)$ and $\mathcal{G}_{\lambda, P_2}(S)$, where the polygons P_1 and P_2 are as in the column on the left. The corresponding graphs of $\mathcal{G}_{\lambda, P_1}(S)$ and $\mathcal{G}_{\lambda, P_2}(S)$, for $\lambda \in [0, 10]$, are also given.

Definition 4. Let a shape S , whose centroid coincides with the origin and scaled to have its area equal to 1, be given. Fix $\lambda > 0$. Let the polygon

$$P(S) = \frac{\text{conv}(S)}{\sqrt{\text{Area}(\text{conv}(S))}} \quad (18)$$

be positioned such that its centroid coincides with the origin. The $\mathcal{C}_\lambda(S)$ convexity measure is defined as:

$$\mathcal{C}_\lambda(S) = \mathcal{G}_{\lambda, P(S)}(S), \quad (19)$$

where the polygon $P(S)$ is defined as in (18).

Similarly as in the sections dedicated to the measures $\mathcal{G}_P(S)$ and $\mathcal{G}_{\lambda, P}(S)$, it can be shown that the measures from the family $\mathcal{C}_\lambda(S)$ have the properties listed in the statement of the following theorem.

Theorem 4. Fix $\lambda > 0$. The convexity measure $\mathcal{C}_\lambda(S)$, defined as in (19), has the following properties:

- (a) $\mathcal{C}_\lambda(S) \in (0, 1]$, for all the shapes S ;
- (b) $\mathcal{C}_\lambda(S) = 1$ if and only if the shape S is convex;
- (c) $\mathcal{C}_\lambda(S)$ is invariant with respect translation, rotation and scaling transformations.

Proof. The proof of (a) and (b) follows from Theorem 2. The measure $\mathcal{C}_\lambda(S)$ is translation and rotation invariant because all the shape measures from the family $\mathcal{G}_{\lambda, P}(S)$ are such an invariant, including the measures from the sub-family \mathcal{C}_λ . \square

Seventh Experiment: The behavior of the measures from the $\mathcal{C}_\lambda(S)$ family. The experiments related to the behavior of the new convexity measures, from the family $\mathcal{C}_\lambda(S)$, are in the Fig.12. Six shapes, and their convex hulls (presented by disjoint line segments), are displayed. The graphs of $\mathcal{C}_\lambda(S)$, for $\lambda \in [0, 5]$, are on the right of the related shapes. By the definition, $\mathcal{C}_{\lambda=0}(S) = 1$, for all the shapes. The values of $\mathcal{C}_\lambda(S)$ decrease, as λ increases. This implies that a higher λ penalizes more strongly the deviations of the considered shapes from their convex hulls. In other words, a

larger λ provides a more sensitive convexity measure, while a smaller λ provides a more robust convexity measure. The largest decrease, in the measured convexity $\mathcal{C}_\lambda(S)$, was in the case of the third shape in the first column. This shape has big holes and deviations from the convex shape inside the shape. Once the holes are removed (the second shape in the first row) the shape becomes nearly convex, and decrease had slowed. Indeed, for $\lambda = 1$, the $\mathcal{C}_\lambda(S)$ is very high ($= 0.9701$). Shape deviations, from a convex shape, become easily visible if $\lambda = 5$ would be selected – in this case $\mathcal{C}_\lambda(S) = 0.7255$.

The shapes in the second row have similar convexity measures, measured by $\mathcal{C}_\lambda(S)$, for all λ . The first shape is a noise free one, while the second one has noise added to the shape boundary. The very similar convexity measures obtained illustrates that the measures $\mathcal{C}_\lambda(S)$ are robust. This is as expected since the measures considered are area based ones - i.e. use both interior and boundary shape points for the computation. The example of the second shape in the third row is illustrative in the following way. This is a shape with a big protrusion. The well known convexity measures, $\mathcal{R}_a(S)$ and $\mathcal{R}_b(S)$, based on a comparison of the shapes given with their convex hull will assign the following convexity measure to this shape:

- $\mathcal{R}_a(S) = \frac{\text{Area}(S)}{\text{Area}(\text{CH}(S))} \approx \frac{2}{3} \approx 0.6667$
- $\mathcal{R}_b(S) = \frac{\text{Perimeter}(\text{CH}(S))}{\text{Perimeter}(S)} \approx \frac{3 + \sqrt{5}}{6} \approx 0.8727$.

Since $\mathcal{C}_\lambda(S)$ varies through $[0.5513, 1]$ for $\lambda \in [0, 5]$, it can be seen that a suitable choice of λ can suit both preferences, either convexity equal to 0.6667 (satisfied by $\mathcal{R}_a(S)$) or 0.8727 (satisfied by $\mathcal{R}_b(S)$). This illustrates the sensibility possibilities of the measures from the family $\mathcal{C}_\lambda(S)$.

7 EXPERIMENTS ON A KNOWN DATA SET

In this section we demonstrate the usefulness of the new shape family measures in an application task on the well

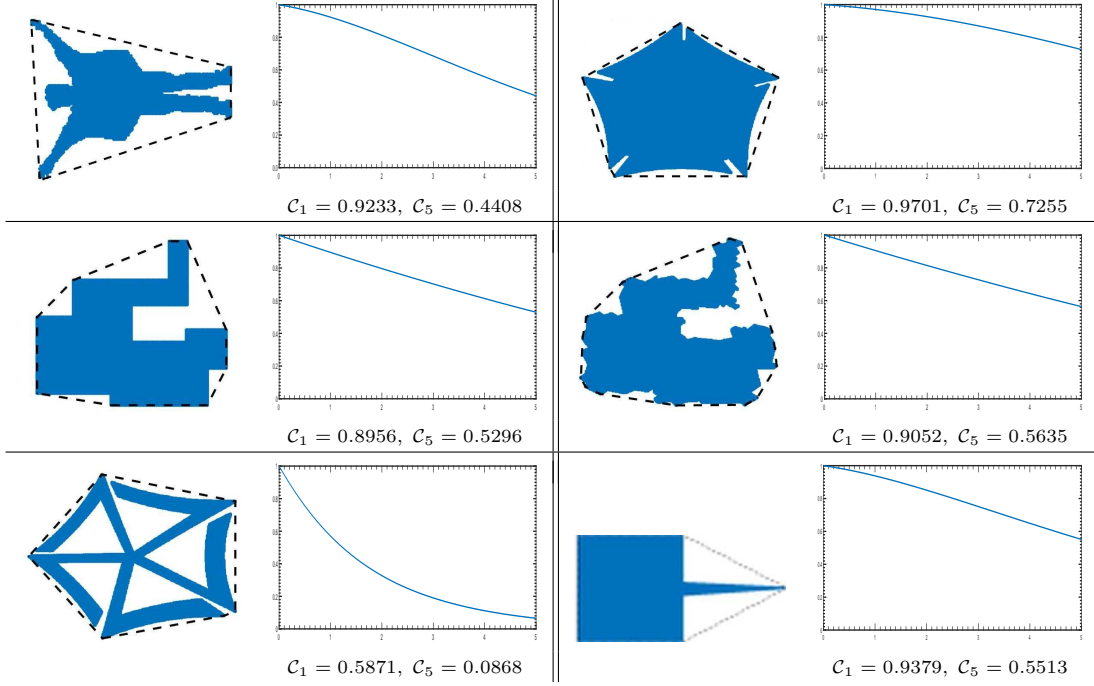


Fig. 12. Six shapes and their convex hulls are displayed. The graphs of their convexities $C_\lambda(S)$ are also given, for $\lambda \in [0, 5]$.

know diatoms data set. In order to put the new measures in a wider context we perform a number of experiments on the same data sets. These experiments involve a number of the known shape measures (and different combinations of them), showing that the new measures are compatible with the existing measures and can be combined with some of them to overcome the benchmark results. But first we make a short discussion related to the well-known shape measure that can be obtained by comparing the union and intersections of the two shapes observed.

Definition 5. Fix a unit area shape \mathbf{Q} . Let S be an arbitrary shape, whose area is also equal to 1 and whose centroid coincides with the centroid of \mathbf{Q} . Then, the shape measure $IoU_{\mathbf{Q}}(S)$ is defined as follows:

$$IoU_{\mathbf{Q}}(S) = \max_{\alpha \in (0, 2\pi]} \left\{ \frac{Area(\mathbf{Q} \cap S(\alpha))}{Area(\mathbf{Q} \cup S(\alpha))} \right\} \quad (20)$$

Such a measure might be understood as a similar one to the new measures, in terms of the computation (an optimization process over an interval of angles) and the use of a function defined over all the planar domain. In the case of the $IoU_{\mathbf{P}}(S)$ measure, the supporting function is defined to be equal to 1, inside the shape \mathbf{Q} , and equal to 0 otherwise. The

e.g. invariance with respect to the similarity and scaling transformation, but also properties that $\mathcal{G}_{\mathbf{Q}}(S)$ does not have; for example $IoU_{\mathbf{Q}}(S) = IoU_{\mathbf{S}}(Q)$, while for a given measure $\mathcal{G}_{\mathbf{Q}}(S)$, the quantity $\mathcal{G}_{\mathbf{S}}(Q)$ is not defined if S is not a convex polygon (this is because non-convex shapes cannot be represented as a set-intersection of a number of hyperplanes, as it has been used in (10)).

As such, $IoU_{\mathbf{Q}}(S)$ is frequently used, but it still cannot perform well in all the applications. The measure $IoU_{\mathbf{Q}}(S)$ does not have a tuning parameter and its behavior is fully determined by the fixed shape \mathbf{Q} (whereas $\mathcal{G}_{\lambda, \mathbf{Q}}(S)$ can be controlled using the parameter λ). Another drawback follows directly from the definition of $IoU_{\mathbf{Q}}(S)$. If the shapes \mathbf{Q} and S do not intersect, after being placed so that their centroids coincide, then the $IoU_{\mathbf{Q}}(S)$ value is always equal to 0. Some examples are shown in Fig.13. Two letter shapes, two cogwheel shapes (extracted from images of varying quality), and two shirt sketch shapes (sketch lines are assumed to be strips having non-zero area), are chosen. A regular 7-gon has been taken for the reference shape \mathbf{G} . The value $IoU_{\mathbf{Q}}(S)$ is equal to 0 for all the six shapes displayed. Thus, the measure $IoU_{\mathbf{Q}}(S)$ is not able to distinguish between these shapes. On the other hand, the measure $\mathcal{G}_{\mathbf{G}}(S)$ assigns different values to all these shapes, and is thus able to distinguish between both individual shapes, as well as between the three shape categories used (letters, cogwheels, and shirts sketches).



Fig. 13. The reference polygon \mathbf{P} is selected to be a regular 7-gon (on the left). The remaining shapes have $IoU_{\mathbf{P}}(S)$ value equal to 0. Their $\mathcal{G}_{\mathbf{P}}(S)$ values vary, and they are: 0.3088, 0.4024, 0.4408, 0.4631, 0.2443, and 0.2667, respectively.

measure $IoU_{\mathbf{Q}}(S)$ is very generic one. It is defined for any shape \mathbf{Q} and any shape S . $IoU_{\mathbf{Q}}(S)$ has nice properties,

Notice that the measure $IoU_{\mathbf{Q}}(S)$ can be modified to avoid the last mentioned drawback, by removing the requirement that the centroids of \mathbf{Q} and S must coincide. However, under such relaxed conditions the modified measure (i.e. the computation of the maximum in (20)) becomes significantly more computationally expensive [34].

7.1 Applications of the New Measures to the Diatoms Classification

We show the incorporation of the proposed shape measure to the classification of diatoms (unicellular algae), which can be used for diverse applications such as forensics [16] and environmental change [27]. The dataset was curated by the ADIAC project [6], and consists of 808 images, each containing a single diatom which is labelled as coming from one of 38 taxa (classes). We follow the procedure from [34], and extract the boundary contours, and also each diatom's ornamentation, which consists of zero or more (mainly open) curve sections in the interior – see Fig.14. Following this, [34] extracted the set of shape descriptors used in [47]³ along with a new convexity measure, Convexification with Fliturn C_{FT} . The latter, additional shape measure provided a small boost in the classification rate from 90.59% to 91.58% as long as the exterior convexity feature was removed – see table 1. Classification was performed using a nearest neighbour classifier with Mahalanobis distances and leave-one-out cross validation.⁴

We take this set of features (14 shape features plus interior convexity plus C_{FT}) and consider adding instances of the proposed $\mathcal{G}_{\lambda, \mathbf{P}}(S)$ measure, which are selected using sequential floating forward search (SFFS) [29]. Underperforming features can also be removed by SFFS. As described in Section 4, a variety of reference polygons are available.

In these experiments we use the following sets of reference polygons: 1/ basic convex shapes: square, equilateral triangle, and circle (approximated by a 100-sided regular polygon), 2/ convex hull of mean shape, 3/ convex polygons derived from each shape: the convex hull, minimum bounding rectangle (MBR) and minimum bounding triangle (MBT), 4/ optimised reference polygons.

The mean shape is calculated by applying a translation, scaling and rotation to each shape in the dataset such that it is centered at the origin, with unit area, and rotated to align its principal axes with the X axis. The normalised shapes are rasterised, and the images averaged and thresholded to produce the mean shape shown in Fig.15.

A simple randomised algorithm is used to generate optimised reference polygons. We initialise 100 reference polygons using random convex polygons which contain between 3 and 15 points. Each reference polygon is evaluated according to the accuracy of classification of the diatoms using just the shape measure derived from the reference polygon. For this experiment only $\lambda = 1$ was considered. Refinement of each reference polygon is carried out by perturbing its points, and retaining the updates only if

3. In the original experiments, [47] used 14 shape measures for diatom classification: circularity, ellipticity, rectangularity, triangularity [31] aspect ratio, compactness, eccentricity, the first four rotation, translation, and scale moment invariants [37], the first three affine moment invariants [12] plus their new convexity measure applied separately to the interior ornamentation and the outer boundary. The classification accuracies for these features which are listed in table 1 are those recomputed in [34] using a different classifier, thereby improving the original scores reported in [47].

4. We note that if the new and existing global descriptors are used individually in this experiment then classification rates are low. Apart from ellipticity (31.19% accuracy), the remaining descriptors produced classification rates ranged from 10.52% to 21.41%. As stated in the Introduction, the full power of the descriptors is obtained when they are combined as shown in Table 1.

they improve the diatom classification accuracy. When the polygon is perturbed any points inside its convex hull are discarded, so that the reference polygon remains convex. After generation of the reference polygons, SFFS is applied as above to combine a selection of the pre-existing features and the optimised reference polygon features.

We test the effectiveness of the hand-crafted reference polygons (listed as sets 1–3 above), and the optimised reference polygons (set 4). When using sets 1–3, applying SFFS causes the removal of some of the shape measures previously used (circularity, eccentricity, triangularity, one RTS moment invariant, and one affine moment invariant) and the addition of the following new measures $\mathcal{G}_{1, \text{square}}(S)$, $\mathcal{G}_{8, \text{MBR}}(S)$, $\mathcal{G}_{2, \text{mean shape}}(S)$, $\mathcal{G}_{2, \text{triangle}}(S)$. As table 1 shows, this produces an increase in the classification accuracy over the results reported in [34].

Using the optimised reference polygons (set 4) produces a similar classification accuracy to sets 1–3. Four reference polygons are generated, as shown in Fig.16. SFFS has also removed two of the previous shape measures: one RTS moment invariant, and one affine moment invariant.

In addition, the effectiveness of $\mathcal{G}_{\lambda, \mathbf{P}}(S)$ in this classification task is compared against two baseline approaches for measuring distances between specified polygons. The first is the area of overlap between the reference polygon and the test shape. Since the sizes of the reference polygon and the test shapes are normalised prior to their comparisons, this measure is equivalent to the Intersection over Union (IoU) which is commonly used for object detection. The reference polygon and test shapes are normalised to be centered on the origin and have unit area; the reference polygon is rotated to maximise the area of overlap with the test shape. The second baseline is the L_2 distance between the turning functions of two polygons [3], which is a well established metric for comparing polygons. As with the $\mathcal{G}_{\lambda, \mathbf{P}}(S)$ experiment, SFFS is applied to find a combination of the 14 shape features along with the seven overlap or turning angle features respectively (using the same seven reference polygons: square, equilateral triangle, circle, mean shape, convex hull, MBR, and MBT). In both cases, SFFS only added a single overlap or turning angle feature (MBR and square respectively) and also removed one of the 14 shape features. While both approaches provide a small increase on the best classification result in [34] (see table 1), they are significantly outperformed by the $\mathcal{G}_{\lambda, \mathbf{P}}(S)$ features.

A third comparison is made with Nguyen and Hoang's [25] measure of polygonality, which is the degree to which a shape resembles an n -sided polygon of arbitrary (i.e. unspecified) shape. The version employing the L_1 norm was used as it was more stable than the L_2 norm. Polygonality measures were calculated for $n = \{3, 4, 5, 6\}$. After applying SFFS, the score was the same as for the overlap method, and was achieved by removing an ellipticity measure and adding a single polygonality measure with $n = 3$.

8 CONCLUDING REMARKS

Instead of exploiting a certain geometric property (e.g. properties satisfied by circles, ellipses, and lines) or some mathematical identities (Hu invariants, Fourier coefficients, Zernike moments, etc.), we have started with a convex

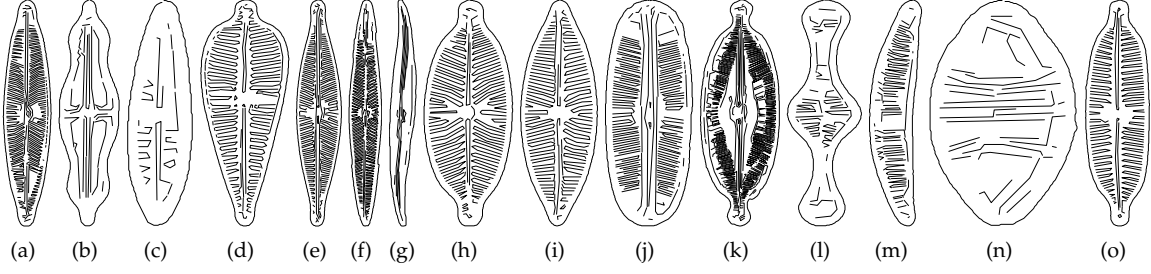


Fig. 14. Outer boundary and interior contours of examples of diatoms from 15 different taxa.

14 shape features	85.77%
14 shape features + interior and exterior convexity	90.47%
14 shape features + interior convexity [47]	90.59%
14 shape features + interior convexity + C_{FT} [34]	91.58%
9 shape features + interior convexity + C_{FT} + \mathcal{G}_λ wrt. 4 reference polygons (from sets 1–3)	94.93%
9 shape features + interior convexity + C_{FT} + \mathcal{G}_λ wrt. 4 reference polygons (from set 4)	94.06%
13 shape features + interior convexity + C_{FT} + overlap wrt. MBR	92.45%
13 shape features + interior convexity + C_{FT} + turning angle distance wrt. square	91.96%
13 shape features + interior convexity + C_{FT} + polygonality	92.45%

TABLE 1

Classification accuracies for diatoms. The reference polygon sets refer to: 1/ basic convex shapes, 2/ convex hull of mean shape, 3/ convex polygons derived from each shape, 4/ optimised reference polygons.



Fig. 15. Estimated mean diatom shape.

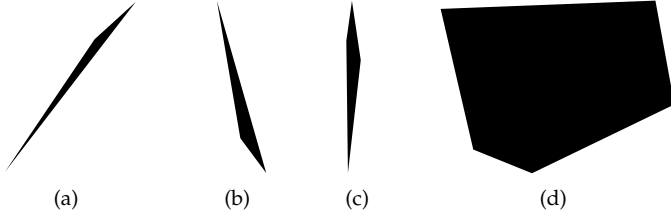


Fig. 16. Optimised reference polygons chosen to maximise diatom classification accuracy.

polygon \mathbf{P} , having a desired shape, and defined a new family of shape measures. We also have involved a tuning parameter λ which controls the sensitivity of the measures from the new family. Each measure $\mathcal{G}_{\lambda, \mathbf{P}}(S)$, from the family, evaluates how much a given shape looks like the selected polygon \mathbf{P} . The shape measures from the family are given in a normalized form, i.e. they all range through the interval $(0, 1]$. Also, the measures are invariant with respect to translations, rotations, and scaling transformations. In addition, each shape measure $\mathcal{G}_{\lambda, \mathbf{P}}(S)$, picks the value 1 if and only if the measured shape S and the polygon \mathbf{P} coincide, independently of the selected λ .

Numerical computation of $\mathcal{G}_{\lambda, \mathbf{P}}(S)$ measures is straightforward, for any choice of the convex polygon \mathbf{P} and the parameter λ . The computational complexity, in practical applications where digital images are used, is discussed.

The method presented allows an extension to 3D shapes. Basically, the equations of the planes that define a 3D convex body, should replace the functions in (4) and the similar

reasoning should be applied as in the 2D case, presented here. Indeed, such analogues of the functions in (4) would have all the properties needed: these would be monotonic functions, taking the value 1 at the reference body surface, would be non-negative but less than 1 inside the body, and bigger than 1 outside of it, etc.

A family of the shape convexity measures is obtained as a corollary of the theoretical framework developed to define $\mathcal{G}_{\lambda, \mathbf{P}}(S)$ measures. If the polygon \mathbf{P} is selected such that $\mathbf{P}(S) = \text{conv}(S) / \sqrt{\text{Area}(\text{conv}(S))}$, then the quantity $\mathcal{G}_{\lambda, \mathbf{P}(S)}(S)$ evaluates how much the shapes of S and its convex hull $\text{conv}(S)$ differ. All the convexity measures $\mathcal{C}_\lambda(S) = \mathcal{G}_{\lambda, \mathbf{P}(S)}(S)$ are also given in the normalized form, i.e. $\mathcal{C}_\lambda(S) \in (0, 1]$. They are invariant with respect to rotations, translations, and scaling transformations, and pick the value 1 if and only if the considered shape is convex. The new convexity measures are robust, and their behavior can be tuned by the parameter λ , in the sense that, for a larger λ , the measure $\mathcal{G}_{\lambda, \mathbf{P}(S)}(S)$ more strongly penalizes the deviation of the shape S from its convex hull $\text{conv}(S)$.

A number of experiments are provided in order to support the statements from the paper, to illustrate the behavior of the new shape measures, and to show their performance in practical applications.

ACKNOWLEDGMENT

The work of J. Žunić is supported by the Serbian Ministry of Sciences. We thank Thanh Phuong Nguyen for providing code for computing polygonality.

REFERENCES

- [1] M.A. Aktaş, J. Žunić: "A Family of shape ellipticity measures for galaxy classification," *SIAM J. Imaging Sciences*, 6:765–781, 2013.
- [2] O. Arandjelović: "Computationally efficient application of the generic shape illumination invariant to face recognition from video," *Pattern Recognition*, 45:92–103, 2012.

- [3] E.M. Arkin, L.P. Chew, D.P. Huttenlocher, K. Kedem, J.S.B. Mitchell: "An efficiently computable metric for comparing polygonal shapes," *IEEE Trans. Patt. Anal. Mach. Intell.*, **13**:209–216, 1991.
- [4] L. Boutsen, C. Marendaz: "Detection of shape orientation depends on salient axes of symmetry and elongation: Evidence from visual search," *Perception & Psychophysics*, **63**:404–422, 2001.
- [5] E. T. Bowman, K. Soga, T. Drummond: "Particle shape characterization using Fourier analysis," *Geotechnique*, **51**:545–554, 2001.
- [6] H. du Buf, M. Bayer, S. Droop, S. Fisher, H. Bunke, M. Wilkinson, J. Roerdink, H. Shahbazkia, A. Ciobanu: "Diatom Identification: a Double Challenge Called ADIAC," In: 10th Int. Conf. on Image Analysis and Processing, pp. 734–739, 1999.
- [7] C.P. Chambers, A.D. Miller: "A measure of bizarreness," *Quarterly Journal of Political Science*, **5**:27–44, 2010.
- [8] H. Davenport: "On a principle of Lipschitz," *J. London Math. Soc.*, **26**:179–183, 1951.
- [9] R.O. Duda, P.E. Hart, D.G. Stork: *Pattern Classification*, New Jersey: Wiley, 2000.
- [10] Y. Dupain, T. Kamae, M. Mendés: "Can one measure the temperature of a curve?" *Archive for Rational Mechanics and Analysis*, **94**:155–163, 1986.
- [11] S.M. Elshoura, D.B. Megherbi: "Analysis of noise sensitivity of Tchebichef and Zernike moments with application to image watermarking," *J. Vis. Commun. Image R.*, **24**:567–578, 2013.
- [12] J. Flusser, T. Suk: "Pattern recognition by affine moment invariants," *Pattern Recognition*, **26**:167–174, 1993.
- [13] J. Flusser, B. Zitova, T. Suk: "Moments and moment invariants in pattern recognition," John Wiley & Sons, 2009.
- [14] T. Gautama, D.P. Mandić, M.M. Van Hulle: "Signal nonlinearity in fMRI: A comparison between BOLD and MION," *IEEE Trans. Medical Images*, **22**:636–644, 2003.
- [15] E. Grisan, M. Foracchia, A. Ruggeri: "A novel method for the automatic grading of retinal vessel tortuosity," *IEEE Trans. Medical Imaging*, **27**:310–319, 2008.
- [16] B.P. Horton, S. Boreham, C. Hillier: "The development and application of a diatom-based quantitative reconstruction technique in forensic science," *Journal of Forensic Sciences*, **51**:643–650, 2006.
- [17] M. Hu: "Visual pattern recognition by moment invariants," *IRE Trans. Information Theory*, **8**:179–187, 1961.
- [18] M.N. Huxley, R. Klette, J. Žunić: Precision of Geometric Moments in Picture Analysis, chapter in Geometric Properties from Incomplete Data, editors: R. Klette, R. Kozera, L. Noakes, J. Weickert, pp. 221–235, Kluwer Publisher, 2006.
- [19] A.K. Jain, A. Vailaya: "Shape-based retrieval: a case study with trademark image databases," *Pattern Recognition*, **31**:1369–1390, 1998.
- [20] K. Misztal, J. Tabor: "Ellipticity and circularity measuring via Kullback-Leibler divergence," *J. Math. Imaging Vis.*, **55**:136–150, 2016.
- [21] L. Kopanja, D. Žunić, B.B. Lončar, G. Saso, M.M. Tadić: "Quantifying shapes of nanoparticles using modified circularity and ellipticity measures," *Measurement*, **92**:252–263, 2016.
- [22] D.R. Lee, T. Sallee: "A method of measuring shape," *Geographical Review*, **60**:555–563, 1970.
- [23] S. Lekshmi, K. Revathy, S.R. Prabhakaran Nayar: "Galaxy classification using fractal signature," *Astronomy & Astrophysics*, **405**:1163–1167, 2003.
- [24] Y. Mei, D. Androutsos: "Robust affine invariant region-based shape descriptors: The ICA Zernike moment shape descriptor and the whitening Zernike moment shape descriptor," *IEEE Signal Processing Letters*, **16**:877–880, 2009.
- [25] T. P. Nguyen, V. THoang: "Projection-based polygonality measurement," *IEEE Transactions on Image Processing*, **24**:305–315, 2015.
- [26] V.N. Nikolić, V. Spasojević, M. Panjan, L. Kopanja, A. Mraković, Marin Tadić: "Re-formation of metastable ϵ -Fe₂O₃ in post-annealing of Fe₂O₃/SiO₂ nanostructure: Synthesis, computational particle shape analysis in micrographs and magnetic properties," *Ceramics International*, **43**:7497–7507, 2017.
- [27] C.A. Paul, K.M. Rühland, J.P. Smol: "Diatom-inferred climatic and environmental changes over the last 9000 years from a low Arctic (Nunavut, Canada) tundra lake," *Palaeogeography, Palaeoclimatology, Palaeoecology*, **291**:205–216, 2010.
- [28] D. Proffitt: "The measurement of circularity and ellipticity on a digital grid," *Pattern Recognition*, **15**:383–387, 1982.
- [29] P. Pudil, J. Novovicova, J.V. Kittler: "Floating search methods in feature-selection," *Pattern Recognition Letters*, **15**:1119–1125, 1994.
- [30] E. Rahtu, M. Salo, J. Heikkilä: "A new convexity measure based on a probabilistic interpretation of images," *IEEE Trans. Patt. Anal. Mach. Intell.*, **28**(9):1501–1512, 2006.
- [31] P.L. Rosin: "Measuring shape: Ellipticity, rectangularity, and triangularity," *Machine Vision Applications*, **14**:172–184, 2003.
- [32] P.L. Rosin, C.L. Mumford: "A symmetric convexity measure," *Computer Vision and Image Understanding*, **103**:101–111, 2006.
- [33] P.L. Rosin, J. Žunić: "Measuring squareness and orientation of shapes," *J. Math. Imaging Vis.*, **39**:13–27, 2011.
- [34] P.L. Rosin, J. Žunić: "Measuring convexity via convex polygons," *LNCS:PSIVT Workshops*, **9555**:38–47, 2015.
- [35] J. Russell, N. Hasler, R. Klette, B. Rosenhahn: "Automatic track recognition of footprints for identifying cryptic species," *Ecology*, **90**:2007–2013, 2009.
- [36] A.W.M. Smeulders, M. Worring, S. Santini, A. Gupta, R. Jain: "Content-based image retrieval at the end of the early years," *IEEE Trans. Patt. Anal. Mach. Intell.*, **12**:1349–1380, 2000.
- [37] M. Sonka, V. Hlavac, V. R. Boyle: *Image Processing, Analysis, and Machine Vision*, PWS, 1998.
- [38] M. Stojmenović, A. Nayak, J. Žunić: "Measuring linearity of planar point sets," *Pattern Recognition*, **41**:2503–2511, 2008.
- [39] J.W.H. Tangelder, R.C. Velkamp: "A survey of content based 3d shape retrieval methods," In Proc. Shape Modeling Applications, pp. 145–156, 2004.
- [40] C.-H. Teh, R.T. Chin: "On image analysis by the methods of moments," *IEEE Trans. Patt. Anal. Mach. Intell.*, **10**:496–513, 1988.
- [41] V.M. Tikhomirov: *Stories about Maxima and Minima*, Providence, RI: Amer. Math. Soc., 1991.
- [42] A.Q. Tool: "A method for measuring ellipticity and the determination of optical constants of metals," *Phys. Rev. (Series I)*, **31**:1–25, 1910.
- [43] B. Wang: "Shape retrieval using combined Fourier features," *Optics Communications*, **284**:3504–3508, 2011.
- [44] J. Xie, G. Dai, F. Zhu, E.K. Wong, Y. Fang: "Deepshape: Deep-learned shape descriptor for 3D shape retrieval," *IEEE Trans. Patt. Anal. Mach. Intell.*, **39**:1335–1345, 2017.
- [45] D. Xu, H. Li: "Geometric moment invariants," *Pattern Recognition*, **41**:240–249, 2008.
- [46] J. Žunić, K. Hirota, P.L. Rosin: "A Hu invariant as a shape circularity measure," *Pattern Recognition*, **43**:47–57, 2010.
- [47] J. Žunić, P.L. Rosin: "A new convexity measurement for polygons," *IEEE Trans. Patt. Anal. Mach. Intell.*, **26**:923–934, 2004.
- [48] J. Žunić, D. Žunić: "A shape interpretation of second shape moment invariants," *J. Math. Imaging Vis.*, **56**:125–136, 2016.



Joviša Žunić is a professor at the Mathematical Institute, Serbian Academy of Sciences. His research interests are in the pattern recognition, shape analysis, image processing, computer vision, neural networks theory, discrete and computational geometry, combinatorics, multivalued logic, and number theory.



Paul L. Rosin is a professor at the School of Computer Science & Informatics, Cardiff University. His research interests include the representation, segmentation, and grouping of curves, knowledge-based vision systems, early image representations, low level image processing, machine vision approaches to remote sensing, methods for evaluation of approximation algorithms, medical and biological image analysis, mesh processing, non-photorealistic rendering and the analysis of shape in art and architecture.